mathematics

MDPI

Article

Predicting and Enhancing the Multiple Output Qualities in Curved Laser Cutting of Thin Electrical Steel Sheets Using an Artificial Intelligence Approach

Muhamad Nur Rohman [1], Jeng-Rong Ho [2], Chin-Te Lin [2], Pi-Cheng Tung [2] and Chih-Kuang Lin [2,*]

[1] Department of Mechanical Engineering, Maarif Hasyim Latif University, Jawa Timur 61257, Indonesia; muhamad.nur.rohman@dosen.umaha.ac.id
[2] Department of Mechanical Engineering, National Central University, Jhong-Li District, Tao-Yuan City 32001, Taiwan; jrho@ncu.edu.tw (J.-R.H.); chintelin@ncu.edu.tw (C.-T.L.); t331166@cc.ncu.edu.tw (P.-C.T.)
* Correspondence: t330014@cc.ncu.edu.tw

Abstract: This study focused on the efficacy of employing a pulsed fiber laser in the curved cutting of thin, non-oriented electrical steel sheets. Experiments were conducted in paraffinic oil by adjusting the input process parameters, including laser power, pulse frequency, cutting speed, and curvature radius. The multiple output quality metrics included kerf width, inner and outer heat-affected zones, and re-welded portions. Analyses of the Random Forest Method and Response Surface Method indicated that laser pulse frequency was the most important variable affecting the cut quality, followed by laser power, curvature radius, and cutting speed. To improve cut quality, an innovative artificial intelligence (AI) approach incorporating a deep neural network (DNN) model and a modified equilibrium optimizer (M-EO) was proposed. Initially, the DNN model established correlations between input parameters and cut quality aspects, followed by M-EO pinpointing optimal cut qualities. Such an approach successfully identified an optimal set of laser process parameters, even beyond the specified process window from the initial experiments on curved cuts, resulting in significant enhancements confirmed by validation experiments. A comparative analysis showcased the developed models' superior performance over prior studies. Notably, while the models were initially developed based on the results from curved cuts, they proved adaptable and capable of yielding comparable outcomes for straight cuts as well.

Keywords: laser cutting; thin electrical steel sheet; curved cut; deep neural network; modified equilibrium optimizer

MSC: 65K05; 65K10; 90C29; 90C59

check for updates

Citation: Rohman, M.N.; Ho, J.-R.; Lin, C.-T.; Tung, P.-C.; Lin, C.-K. Predicting and Enhancing the Multiple Output Qualities in Curved Laser Cutting of Thin Electrical Steel Sheets Using an Artificial Intelligence Approach. *Mathematics* **2024**, *12*, 937. https://doi.org/10.3390/math12070937

Academic Editor: Efstratios Tzirtzilakis

Received: 15 February 2024
Revised: 13 March 2024
Accepted: 18 March 2024
Published: 22 March 2024

1. Introduction

Due to their exceptional magnetic characteristics, non-oriented electrical steels are widely utilized as core materials in small transformers, medium generators, and electric motors. The increasing global emphasis on reducing fossil fuel consumption has led to a growing popularity of electric motors in electric vehicles. The role of non-oriented electrical steel sheets becomes more and more important due to their contributions to improving the efficiency of the electrical motors, including reduction of temperature, energy loss, and cost. The low-electricity-consuming electrical motors can be provided by applying a thin-gauge non-oriented electrical steel sheet for use in rotors and stators. Utilizing thin-gauge non-oriented electrical steel sheets, typically ranging from 0.1 to 0.35 mm in thickness, enhances the efficiency of electrical motors [1].

In the production of electrical machinery, electrical steel sheets are molded and layered to construct the rotor and/or stator components. In the process, cutting results in the largest deterioration of magnetic properties in all the steps [2]. For mass production of electrical steel sheets, mechanical cutting is the most advantageous method due to its low cost and good repeatability. However, mechanical cutting is usually performed on thick metal sheets, which are generally thicker than 0.35 mm due to their tendency to bend under shear force. The laser process has emerged as a favorable option for cutting thin non-oriented electrical steel sheets. Its non-contact method eradicates vibrations and machine noises. Moreover, laser cutting offers several benefits, including the capability to produce intricately shaped parts with exceptional precision, adaptability to design modifications, and cost-effectiveness in fixture and tool preparation. Unlike mechanical cutting, laser cutting prevents plastic deformation near the cutting edge. Furthermore, laser cutting surpasses mechanical cutting in terms of magnetic performance when used for electrical steel sheets [3]. However, magnetic deterioration after laser cutting has been reported in various studies [3,4]. Heat-affected zone (HAZ) is a region in a material, typically metal, that has experienced changes in its microstructure and properties due to exposure to high-temperature thermal cutting processes. These changes occur adjacent to the heat source and can include alterations in material properties. Magnetic deterioration is more pronounced in laminated cores with a wider HAZ [3,4]. Furthermore, laminates with a wider kerf result in a larger core loss [3]. In addition, the recast layers may rejoin during laser cutting, closing the kerf and causing re-welding [5,6].

The efforts to optimize cut quality in electrical steel sheets, including HAZ, kerf width, and re-welded portion, have been conducted in several studies [4,5,7–9]. Nguyen et al. [4] and Rohman et al. [7] minimized the HAZ and kerf width, respectively, by optimizing the laser process parameters for straight cuts of non-oriented electrical steel sheets. By controlling the working temperature during laser cutting, Nguyen et al. [8] reduced the kerf width and HAZ of straight cuts of electrical steel sheets. A laser process parameter optimization technique based on image processing was used to eliminate re-welded cuts in the circular cutting of electrical steel sheets [5].

The heat energy and transport phenomena during laser cutting are influenced by the interaction between the material, the incident laser beam, and the environment, which vary based on the laser process parameters. It includes, for example, light absorption, heat conduction, melting, vaporization, plasma formation, energy loss by conduction, and convection and radiation and, consequently, affects the cut quality. The mechanism underlying laser cutting is fundamentally complicated, and the intricate, nonlinear relationships between its parameters make it challenging for researchers to model the process accurately [10].

Artificial intelligence (AI) models, including adaptive neuro-fuzzy inference system (ANFIS), artificial neural network (ANN), and generalized regression neural network (GRNN), have been utilized to solve and anticipate numerous intricate engineering issues. Such AI-based models are employed to predict cut qualities (outputs) by considering laser process parameters (inputs). Several investigations employed ANN to predict cut qualities in laser cutting of PMMA and electrical steel sheets [7,11,12]. Ding et al. [13] utilized GRNN to anticipate surface roughness and kerf width in the laser cutting of 304L plates. The use of ANFIS was reported by Rajamani et al. [14] on laser cutting of Hastelloy C276 sheets. Deep neural networks (DNNs) have become popular due to their superiority over shallow neural networks (SNNs) and other machine learning algorithms [7,11]. However, using an inappropriate number of hidden layers in a DNN may result in lower prediction accuracy compared to SNN and other machine learning algorithms.

Metaheuristic optimization methods, such as grey wolf optimization (GWO), genetic algorithm (GA), particle swarm optimization (PSO), and equilibrium optimizer (EO), have been applied to optimize output quality, by finding the optimal processing parameters. In various studies, GWO, GA, and PSO methods were successfully used to optimize laser cutting processes and other engineering problems using AI-based models as objective functions. Rohman et al. [11] employed a combination of a DNN and GWO to optimize five cut-quality characteristics during laser cutting of electrical steel sheets under varying environmental conditions. DNN models and GA were applied to reduce roundness and kerf width during the laser cutting of electrical steel sheets [7]. Sibalija et al. [15] utilized one-hidden-layer ANN and PSO to optimize seven characteristics of cut quality for laser cutting of Nimonic 263 alloy sheets. Guo et al. [16] used support vector regression (SVR) and GA to optimize initial residual stress for ultra-precision machining of thin-walled pure copper. In addition, the GA, GWO, and EO have been successfully applied to determining the hyperparameters of various AI-based models [7,11,17].

Based on the available literature, there is still a lack of studies that minimize HAZ, kerf width, and re-welded portions simultaneously for laser cutting of thin non-oriented electrical steel sheets with curved paths. Simultaneously optimizing the HAZ, kerf width, and re-welded portions during laser cutting is essential to determine the optimal laser process parameters that lead to minimizing these aspects. A study on laser cutting of thin non-oriented electrical steel sheets with curved paths is necessary since the curvature radius plays a key role in determining the cut quality [18]. Accordingly, this study focused on the use of AI-based approaches to predicting and enhancing the cut quality in the curved laser cutting of non-oriented electrical steel sheets. SNN, DNN, GRNN, and ANFIS were first developed and compared for their performance in predicting multiple characteristics of cut quality. To develop the AI-based models, a full factorial experimental design was conducted considering curvature radius (R), laser power (P), laser pulse frequency (f), and cutting speed (v) as input parameters. Kerf width, inner HAZ, outer HAZ, and re-welded portion were measured and considered as output quality characteristics. The experiments were performed in a paraffinic oil environment, as it demonstrated superiority over air and alcohol environments [11]. A novel modified EO (M-EO) was devised to determine the laser process parameters that yield the optimal cut quality. In order to improve the ability to reach equilibrium, M-EO procedures were proposed based on particle memory saving and equilibrium pool updating strategies. The robustness of the M-EO algorithm and the superior AI-based model in obtaining the optimal process parameters was confirmed via validation experiments. This study reports a new method to improve the multiple characteristics of cut quality that greatly influence the magnetic properties in curved laser cutting of thin non-oriented electrical steel sheets, which can be applied in industrial practice. Furthermore, the technique suggested in this study has the potential to be applied to thin sheets with a wide range of applications.

2. Experimental Procedures

2.1. Material and Experimental Setup

All experiments took place in paraffinic oil, using a laser configuration consisting of a 20 W pulsed fiber laser system, a laser beam expander, a scanner, and a focusing lens. The laser functioned at a wavelength of 1064 nm, with a pulse frequency varying from 20 to 80 kHz, and a pulse duration of 100 ns. It was focused on a spot measuring 50 µm in diameter on its focal plane. Information regarding the laser system and experimental arrangement was given elsewhere [11]. Thin non-oriented silicon steel sheets, 0.1 mm thick (ST-100, Nikkin Denji Kogyo Co., Ltd., Saitama, Japan), were employed in the study. The experiment involved cutting a 90-degree arc path with radii of 1 mm, 3 mm, and 5 mm using different combinations of laser process parameters. Figure 1 depicts the schematic diagram illustrating the arrangement of the workpiece and environment for laser cutting.

2.2. Design of Experiment

A full factorial experimental design incorporating four factors and three levels was utilized to explore the impact of various process parameters on cut quality. Preliminary experiments were conducted to ascertain the suitable levels for each parameter, ensuring that all trials could achieve a complete cut in the material with a single pass. Table 1 presents the selected levels for the laser process parameters.

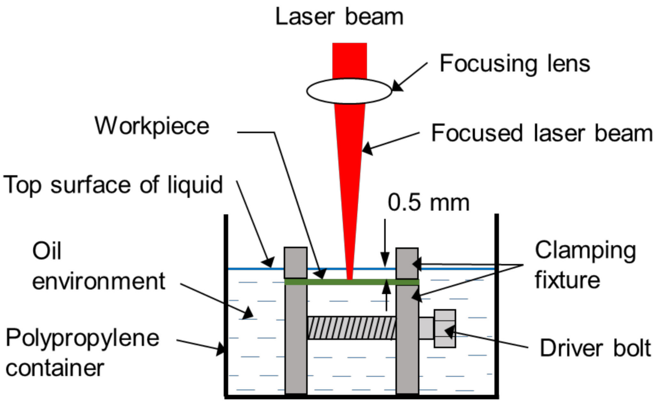

Figure 1. Schematic of the experimental setup for curved laser cutting of thin non-oriented silicon steel sheets.

Table 1. Laser process parameters and their levels used in the experiment.

Parameter	Level 1	Level 2	Level 3
Curvature radius, R (mm)	1	3	5
Laser power, P (W)	12	14	16
Laser pulse frequency, f (kHz)	20	26	32
Cutting speed, v (mm/s)	0.10	0.15	0.20

2.3. Quality Characteristics

Four indices were used to evaluate cut quality, namely, kerf width (Kw), inner HAZ (HAZ_{in}), outer HAZ (HAZ_{out}), and re-welded portion (Rp). The dimensions of Kw, HAZ_{in}, and HAZ_{out} are defined and schematically shown in Figure 2a. The dimensions of Kw, HAZ_{in}, and HAZ_{out} were measured for each sample at 5 locations as illustrated in Figure 2a, and their averages were used as the resulting cut qualities for each sample. The description of Rp is schematically shown in Figure 2b. Note that $Rp = \alpha^\circ/90^\circ$, where α° is schematically defined in Figure 2b. The Kw, HAZ_{in}, and HAZ_{out} were identified through visual examination, employing a method identical to that utilized in [4], which was subsequently verified through microstructural analysis.

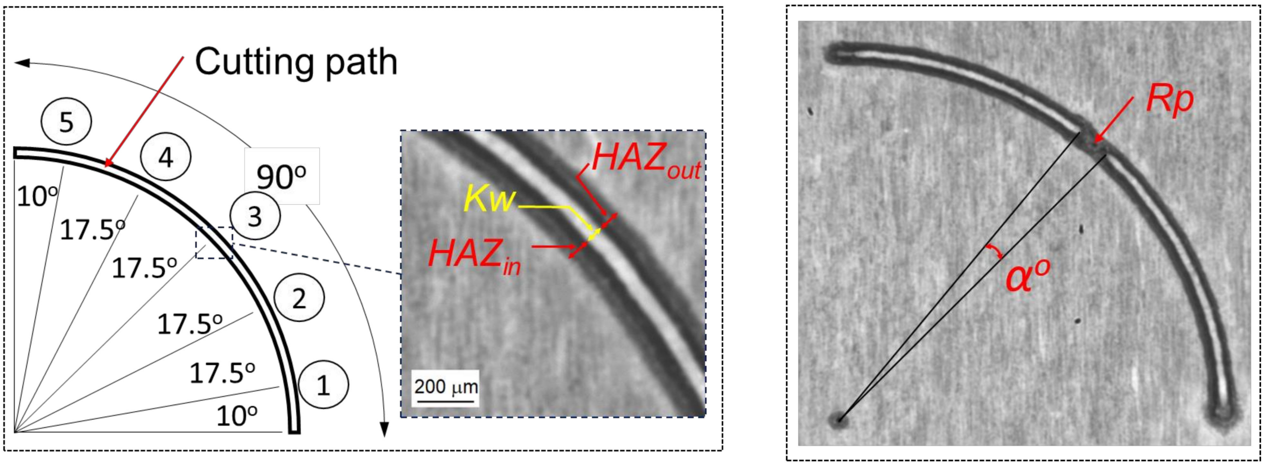

(**a**) (**b**)

Figure 2. Diagram illustrating the (**a**) curved cut profile and the locations for measuring Kw, HAZ_{in}, and HAZ_{out} (left), explanation of Kw, HAZ_{in}, and HAZ_{out} (right) and (**b**) definition of Rp and α°.

All dimensional measurements were conducted employing a computer vision setup, comprising a camera (Cyclops SU1000-8, AISYS Vision Co., Taipei, Taiwan), a lens (Optem MVZL 34-11-10, Optem Inc., Medina, OH, USA), and an LED light source (white light). Measurement via computer vision was carried out using custom-developed software utilizing Python 3.9 (Python Software Foundation, Wilmington, DE, USA) and OpenCV (Open Source Computer Vision Library). The main operation procedures are described as follows:

1. Before measuring the object, perform camera calibration with a metal stage micrometer (OBMM 1/100, OLYMPUS, Tokyo, Japan). This procedure determined the measurement resolution (2.09 µm/pixel).
2. Draw lines for the dimensions of Kw, HAZ_{in}, HAZ_{out}, and Rp. Different colors were used to distinguish Kw, HAZ_{in}, HAZ_{out}, and Rp.
3. Perform image segmentation using the HSV color space.
4. Determine the length of each line for each color. Firstly, convert the image to grayscale and then convert the grayscale image to black and white. The step continued by measuring the length in units of pixels. Finally, to determine the dimensions in the metric unit, multiply the dimensions in pixels by the measurement resolution (µm/pixel) as determined in Step (1).

The measurement results and the corresponding laser process parameters are given in Table S1 of Supplementary Materials. A gray relational analysis (GRA) [19] approach was utilized to quantify and sort the value of cut quality. The best, the average, and the worst cut qualities were found in Experiment Nos. 34, 44, and 18, respectively. Figure 3 shows the cut-quality images of Experiment Nos. 34, 44, and 18. Figure 4 shows the interval plots for HAZ_{in} and HAZ_{out} of the 81 sets of experiments, which were analyzed using the MINITAB 18 software (Minitab, Inc., State College, PA, USA). As shown in Figure 4, HAZ_{in} is significantly larger than HAZ_{out}. During laser cutting, the kerf absorbed the laser energy and transferred it through heat conduction to the material [20]. HAZ_{in} was larger than HAZ_{out} because of lower heat conduction into the material from the inner side of the curved cut and a greater accumulation of heat energy.

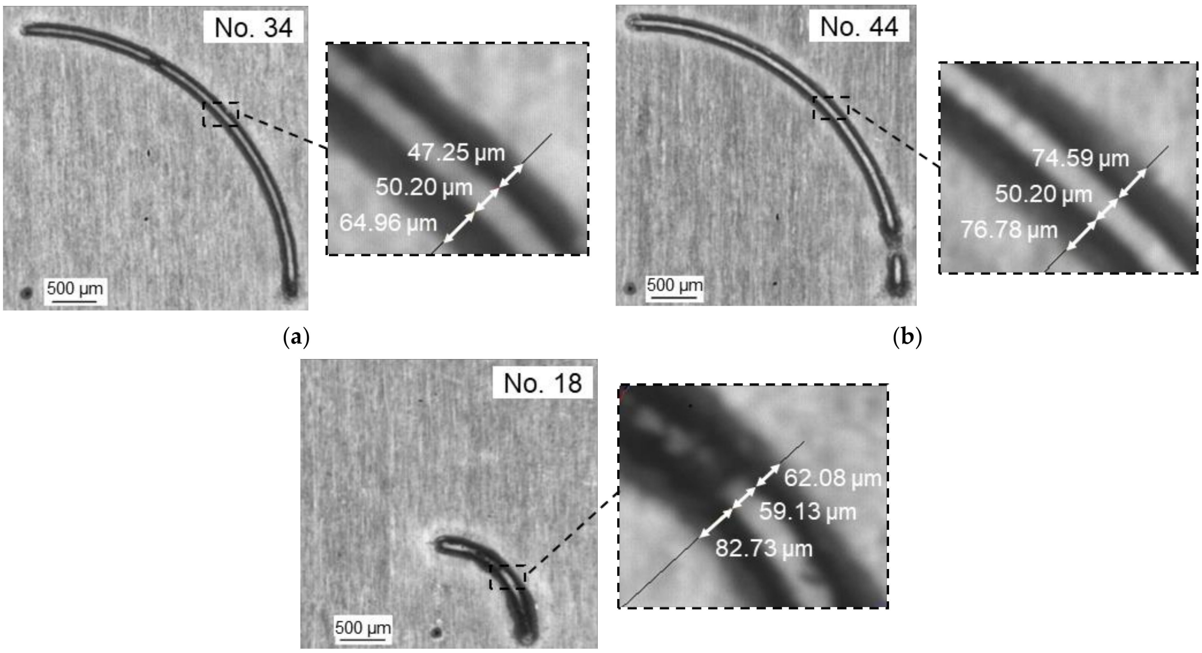

(**a**) (**b**)

(**c**)

Figure 3. Images of (**a**) the best cut quality, (**b**) the average cut quality, and (**c**) the worst cut quality.

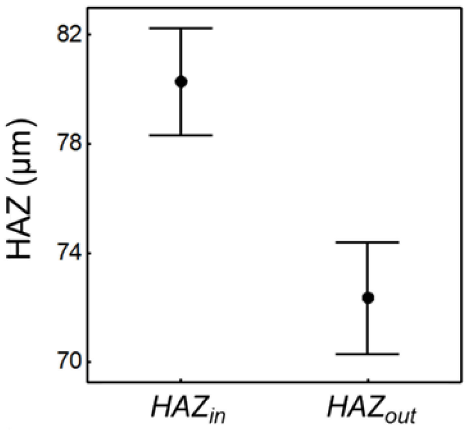

Figure 4. Interval plots for HAZ_{in} and HAZ_{out}.

3. Effects of Laser Process Parameters on Cut Quality

The relative importance of each input parameter in correlation with cut quality was determined using a Random Forest Method (RFM) [21]. The Random Forest Regressor model from the Scikit-learn module in Python 3.9 was specifically used for this task. Figure 5 displays the results. The cut quality was quantified using the normalized cut quality (NCQ), which was computed using the following formula:

$$\mathrm{NCQ} = \frac{1}{4}\frac{Kw}{Kw^{max}} + \frac{1}{4}\frac{HAZ_{in}}{HAZ_{in}^{max}} + \frac{1}{4}\frac{HAZ_{out}}{HAZ_{out}^{max}} + \frac{1}{4}\frac{Rp}{Rp^{max}} \tag{1}$$

where Kw^{max}, HAZ_{in}^{max}, HAZ_{out}^{max}, and Rp^{max} represent the maximum values observed in the experimental data for Kw, HAZ_{in}, HAZ_{out}, and Rp, respectively. Consequently, a lower NCQ value signifies superior cut quality.

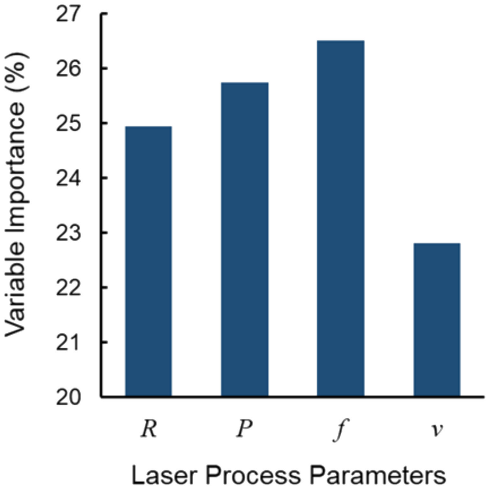

Figure 5. Percentage of variable importance calculated by RFM.

The normalization process in Equation (1) divides each metric by its maximum value to ensure that all cut quality indices are on an equal scale for fair comparison. This normalization is essential to accurately evaluate cut quality because each index varies in range, and it is crucial to ensure that they are all evaluated on the same scale. The motivation behind this normalization is to prevent any individual metric from dominating the NCQ calculation due to differences in their original scales. Without normalization, metrics with larger numerical values would inherently carry more weight in the calculation of NCQ, potentially skewing the results and leading to inaccurate interpretations of cut quality. The weights in Equation (1) were equal, indicating that each quality metric was given an equal value. This decision was made to ensure fairness and balance in evaluating cut quality [7,22,23]. According to Figure 5, the cut quality is most significantly influenced by the laser pulse frequency, followed by the laser power, curvature radius, and cutting speed.

The MINITAB 18 software was utilized to construct Response Surface Method (RSM) models, aiming to investigate the impacts of individual laser process parameters on cut quality. Validation of the RSM models was performed through analysis of variance, demonstrating significant p-values below 0.05. The RSM results are illustrated in Figure 6.

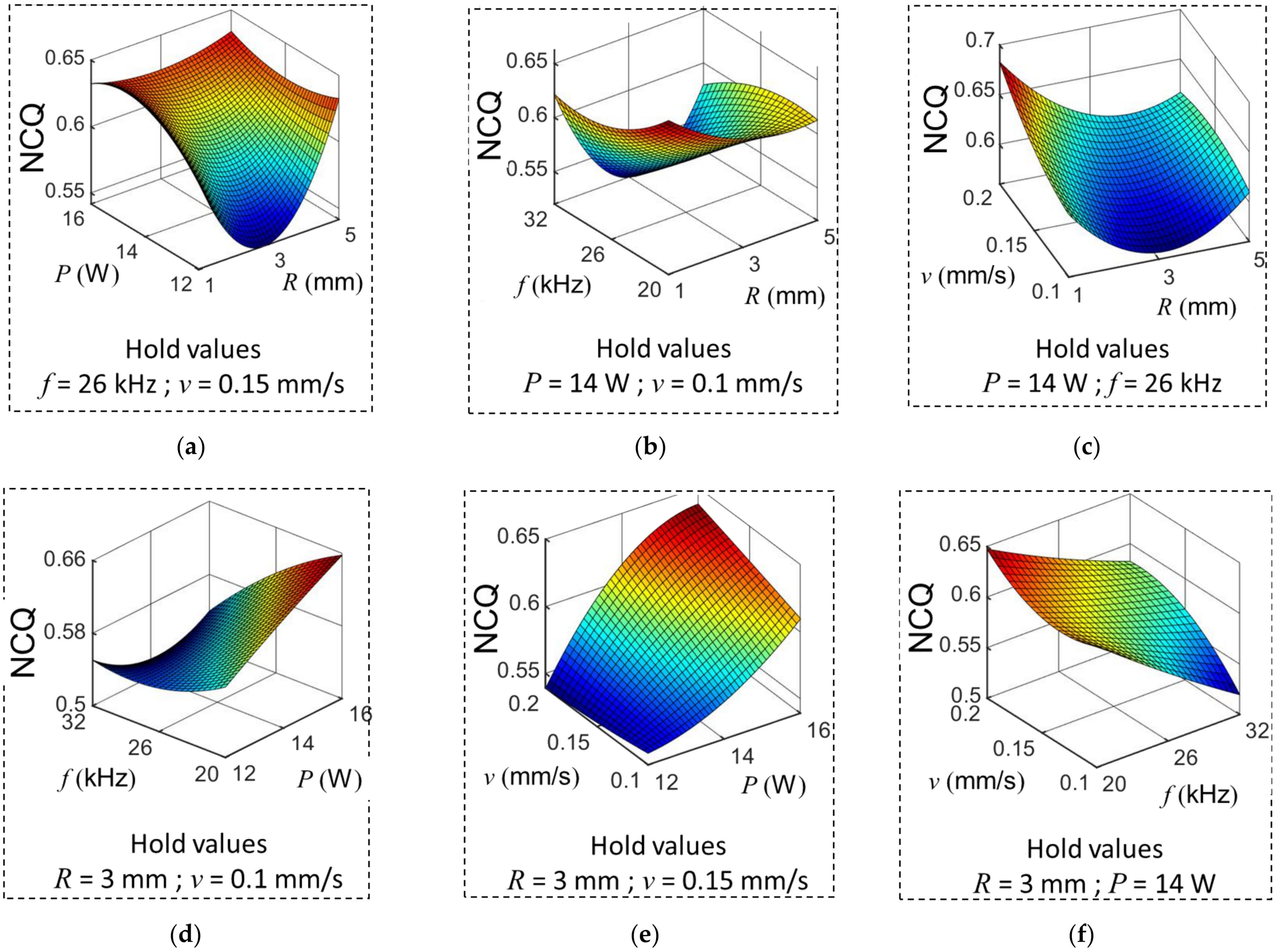

(**a**) (**b**) (**c**)

(**d**) (**e**) (**f**)

Figure 6. Response surface plots of NCQ for various pairs of variables: (**a**) R and P, (**b**) R and f, (**c**) R and v, (**d**) P and f, (**e**) P and v, and (**f**) f and v.

Figure 6a–c demonstrate that as the curvature radius is raised to a critical level, there is a decrease in NCQ. However, NCQ starts to increase again once the curvature radius surpasses this critical value. Cutting with a small curvature radius generates a larger accumulation of heat energy at the kerf due to a smaller area of heat conduction into the material [20]. Consequently, there is an increase in the quantity of molten material, leading to higher kerf width, HAZ, and the formation of a recast layer. A higher value of NCQ for a larger curvature radius greater than the critical one can be attributed to the exothermic reaction with a higher amount of dissolved oxygen in the oil during laser cutting. A larger surface area covered during laser cutting implies a higher concentration of oxygen dissolved in the oil [24]. The presence of dissolved oxygen in the oil triggers exothermic reactions at elevated temperatures within the cutting region, leading to excessive heat generation during the cutting process [25,26].

As depicted in Figure 6a,d,e, raising the laser power typically leads to an increase in NCQ. Employing lower laser power results in less energy being transferred to the kerf, which decreases the amount of molten material [27], consequently reducing kerf width, HAZ, and the volume of the recast layer. Conversely, Figure 6b,d,f demonstrate that increasing the pulse frequency generally lowers the NCQ. Increasing the pulse frequency (f) of laser irradiation results in a decrease in the laser peak power (P_p). It should be noted that $P_p = P_{ave}/tf$, where P_{ave} represents the average power and t represents the pulse duration [27]. As a result, increasing the pulse frequency led to a reduction in the kerf width, HAZ, and thickness of the recast layer.

Figure 6c,e,f demonstrate a positive correlation between increasing the cutting speed and the overall rise in NCQ. Due to the absorption of laser energy by the kerf and its subsequent transfer to the substrate through heat conduction [20], a higher cutting speed minimizes energy loss through heat conduction and maximizes the amount of material that melts. Consequently, the outcome was an increased kerf width, a wider HAZ, and a greater quantity of recast layer.

In summary, both RFM and RSM analyses demonstrate the significant impact of all controlled laser process parameters on cut quality. Therefore, it is affirmed that R, P, f, and v were the suitable input parameters chosen for the AI-based models to predict cut quality. The results of investigating the influence of process parameters on cutting quality can be effectively used to improve the laser cutting process in the industry. This involves adjusting these parameters to their optimal values to minimize the HAZ, kerf width, and re-welded portions.

4. AI-Based Modeling and Optimization

This work involved the development of four AI-based models, specifically SNN, DNN, GRNN, and ANFIS, for the purpose of predicting cut quality. These models utilized laser process characteristics as inputs. The main goals of creating these four models were to assess their effectiveness and determine the most suitable model for accurate predictions of cut characteristics in the given laser processes. A comparative analysis was conducted to establish the optimal model performance. The most superior model was subsequently employed as the objective function in M-EO optimization to acquire the ideal process parameters that result in the highest grade of cut. Figure 7 illustrates the overall process of using AI-based modeling to predict and optimize the quality of the cut. Specifics of each stage are detailed below. The SNN, DNN, GRNN, ANFIS, and M-EO models were created using Python 3.9 code.

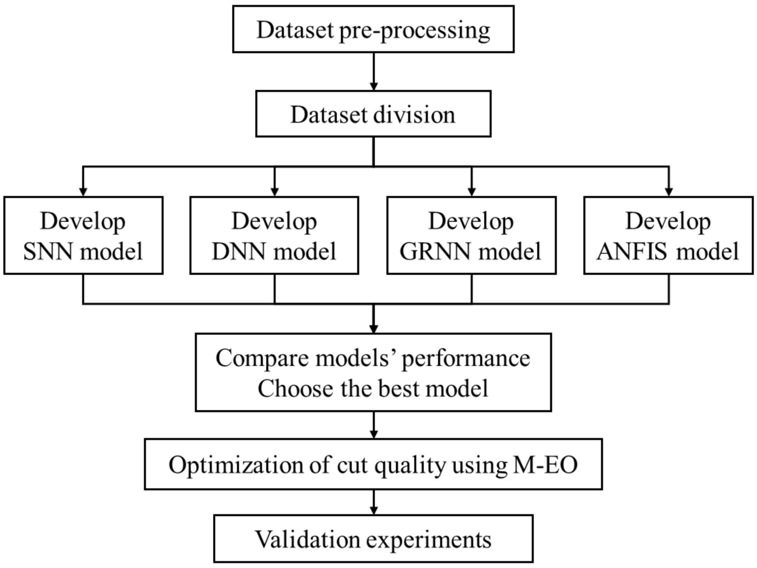

Figure 7. General workflow in AI-based modeling.

4.1. Dataset Pre-Processing

To account for the potential absence of the ideal combination of process parameters inside the process window of the 81 experimental runs, the lower and upper limits of each process parameter were expanded beyond the specified levels for the purpose of normalization. The input and output variables were initially standardized to a range of 0 to 1.

4.2. Shallow Neural Network and Deep Neural Network

An SNN refers to a type of ANN that has a feed-forward structure with only one hidden layer [28]. On the other hand, a DNN, which is also a feed-forward ANN, has several hidden layers [28,29]. Figure 8 provides a schematic representation of the overall architecture of SNN and DNN, which are both built using the Keras framework. The input variables included R, P, f, and v, whilst the output variables encompassed Kw, HAZ_{in}, HAZ_{out}, and Cp. Here, Cp denotes the clean-cut portion, which is determined using the formula Cp = 1-Rp. The hidden neurons utilized the rectified linear unit (ReLU) activation function, while the output neurons employed the sigmoid activation function. ReLU is preferred for hidden neurons due to its simplicity and effectiveness. It addresses the vanishing gradient problem, leading to faster convergence during training. By setting negative input values to zero, ReLU introduces non-linearity, facilitating efficient learning of complex patterns in hidden layers [30]. Using the Sigmoid activation function for output neurons in this application scales the output values between 0 and 1, suitable for representing probabilities or proportions. Sigmoid ensures the output values are bounded within this range, facilitating their interpretation. Additionally, Sigmoid's differentiability supports optimization techniques like back-propagation, aiding in the efficient adjustment of weights and biases during the learning phase [31]. Such choice enhances convergence and training stability in both the SNN and DNN architectures described. The AI-based models were constructed by randomly dividing the datasets into training, validation, and testing sets. The back-propagation algorithm was used to make adjustments to weights and biases during the learning phase, following the Adam optimizer technique.

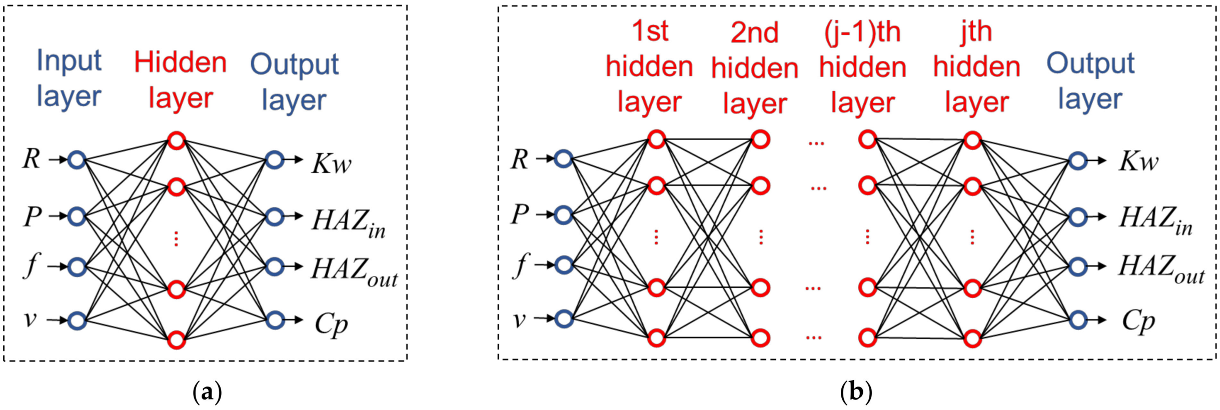

Figure 8. Schematic of (**a**) an SNN model and (**b**) a DNN model.

The training of SNN and DNN consists of two processes. Firstly, a pre-trained model was developed using the EO algorithm [32] by determining the number of neurons, the dropout rate in each hidden layer, and the random seed number. The significant effects of the dropout rate and random seed number on the accuracy of the model have been reported in the literature [33,34]. Secondly, the pre-trained models were then re-trained (fine-tuned) to improve their accuracy.

During the development of the pre-trained model, 60%, 20%, and 20% of the 81 datasets were allocated for training, validation, and testing, respectively. To assess the performance of the SNN and DNN models in generating prediction data, a 5-fold cross-validation (CV) technique was employed during fine-tuning. In this fine-tuning phase, 83% of the 81 datasets were utilized for training and validation within the 5-fold CV, while the remaining 17% were reserved for testing purposes. The utilization of CV offers several advantages, as previously discussed in [35,36].

4.3. Generalized Regression Neural Network

GRNN is a neural network that utilizes radial basis function (RBF) and has a non-linear relationship between input and output variables. The construction of a GRNN consists of four layers: an input layer, a pattern layer, a summation layer, and an output layer. The GRNN in this study follows a similar structure to that described in Reference [13], featuring a single output neuron. The training process of the GRNN is significantly influenced by a smoothing factor (σ). The comprehensive methodology of the GRNN was provided in Reference [13]. The pyGRNN package was utilized to construct the GRNN structure in this investigation. The σ parameter and the random seed number were optimized using a GridSearchCV technique with a 5-fold CV.

4.4. Adaptive Neuro-Fuzzy Inference System

ANFIS combines the principles of ANN and fuzzy logic systems to establish the mathematical connection between input and output variables. Its structure comprises an input layer, a fuzzification layer, a product layer, a normalized layer, a defuzzification layer, and an output layer. The ANFIS structure adopted in this study closely resembles that described in Reference [14]. The detailed procedure for implementing ANFIS was described in Reference [37]. In this study, the ANFIS structure was created using the anfis library. A GridSearchCV technique with a 5-fold CV was also used to optimize the random seed number, the membership functions (gaussian, gbellmf, and sigmoid), and the number of epochs.

4.5. Performance Evaluation of the Developed AI-Based Models

Statistical indicators, specifically the mean absolute percentage error (MAPE) and the absolute fraction of variation (R^2), were utilized to evaluate the effectiveness of the AI-based models [11,38]. When the MAPE value is close to zero and the R^2 value is close to one, the performance of a model is regarded to be superior. The following Equations (2) and (3) were utilized to arrive at these values,

$$\mathrm{MAPE} = \frac{1}{n}\sum_{i=1}^{n}\left|\frac{a_i - p_i}{a_i}\right| \cdot 100\% \tag{2}$$

$$\mathrm{R}^2 = 1 - \left(\frac{\sum\limits_{i=1}^{n}(a_i - p_i)^2}{\sum\limits_{i=1}^{n} p_i^2}\right) \tag{3}$$

where a_i is the expected value, p_i is the predicted value, and n is the number of data. In this study, a_i stands for the ith dataset for parameters Kw, HAZ_{in}, HAZ_{out}, and Rp acquired from experimental observations, while p_i denotes the ith dataset for the same parameters Kw, HAZ_{in}, HAZ_{out}, and Rp, respectively, predicted by the SNN, DNN, GRNN, and ANFIS models. The variable n represents the quantity of data utilized for calculations. The process for calculating MAPE values to evaluate model performance involves the following steps:

1. Calculate the absolute error for each data point by finding the absolute difference between the predicted value (p_i) and the actual value (a_i).
2. Determine the relative error for each data point by dividing the absolute error by the actual value (a_i).
3. Sum up all the relative errors.
4. Divide the total sum of relative errors by the total number of data points (n).
5. Multiply the result by 100% to express it as a percentage.

An SNN and DNNs consisting of 2–6 hidden layers were created as previously explained. The rankings of the SNN's and DNNs' performance after fine-tuning were determined based on their scores, which were computed using the following formula [11]:

$$\text{Score} = \frac{1}{3} f_{e\text{-}training} + \frac{1}{3} f_{e\text{-}validation} + \frac{1}{3} f_{e\text{-}testing} \tag{4}$$

where $f_{e\text{-}training}$, $f_{e\text{-}validation}$, and $f_{e\text{-}testing}$ represent the normalized MAPE values for the training, validation, and testing sets, respectively. They were determined as follows:

$$f_{e_l} = \frac{MAPE_{max} - MAPE_l}{MAPE_{max} - MAPE_{min}} \tag{5}$$

where f_{e_l} represents the normalized MAPE of an SNN or DNN with l hidden layers, $MAPE_{min}$ and $MAPE_{max}$ denote the minimum and maximum MAPE values, respectively, and $MAPE_l$ signifies the MAPE of the SNN or DNN with l hidden layers.

Figure 9 displays the scores of the SNN and DNNs with 2–6 hidden layers. Figure 9 demonstrates that the DNN model with 5 hidden layers achieves the highest score compared to the SNN and other established DNNs. Therefore, the DNN model with 5 hidden layers was used to predict the cut characteristics. The architecture of the DNN consisted of 5 hidden layers with the following number of neurons in each layer: 4-(101-101-113-132-127)-4. It should be noted that the quantity of nodes in each hidden layer is denoted by the numbers included in parentheses in a specific order. The number of nodes in the input layer is shown by the value preceding the parenthesis, whereas the number of nodes in the output layer is indicated by the value after the parenthesis. Table 2 displays the results of the SNN, 5-hidden-layer DNN, GRNN, and ANFIS models' performance. Table 2 demonstrates that the 5-hidden-layer DNN outperforms SNN, GRNN, and ANFIS, as evidenced by its lowest MAPE value and highest R^2 value in training, validation, and testing. The 5-hidden-layer DNN is capable of accurately predicting the cut quality in the curved laser cutting process of thin non-oriented electrical steel sheets. As shown in Table 2, the predictive accuracy of Kw, HAZ_{in}, HAZ_{out}, and Cp is demonstrated by remarkably low MAPE values across their respective training, validation, and testing datasets, with 0.32%, 0.52%, and 0.87% for Kw; 0.23%, 0.38%, and 0.49% for HAZ_{in}; 0.25%, 0.35%, and 0.38% for HAZ_{out}; and 0.23%, 0.34%, and 0.23% for Cp, respectively. Following that, the 5-hidden-layer DNN model was chosen as the objective function in M-EO optimization to identify the optimal process parameters for achieving the highest quality of cut.

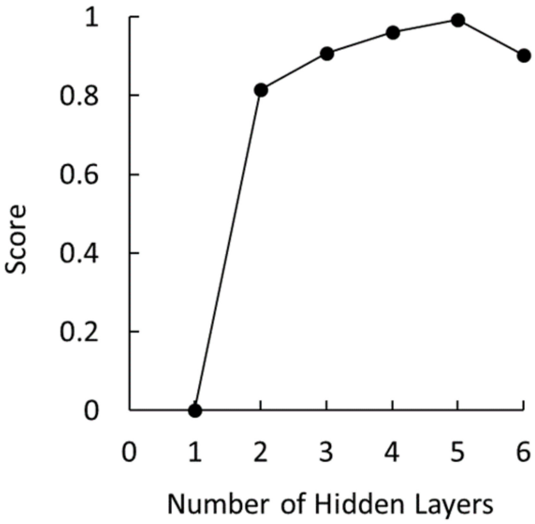

Figure 9. Scores obtained by the SNN and DNNs with varying numbers of hidden layers following fine-tuning.

Table 2. Prediction performance of SNN, 5-hidden-layer DNN, GRNN, and ANFIS.

Quality Index	AI-Based Models	MAPE (%)			R^2		
		Training	Validation	Testing	Training	Validation	Testing
Kw	SNN	2.14	4.21	3.29	0.9986	0.9962	0.9979
	5-hidden-layer DNN	0.32	0.52	0.87	1.0000	0.9999	0.9999
	GRNN	2.36	3.34	4.09	0.9976	0.9948	0.9921
	ANFIS	0.38	3.83	4.87	0.9996	0.9924	0.9896
HAZ_{in}	SNN	1.76	2.51	1.80	0.9990	0.9985	0.9995
	5-hidden-layer DNN	0.23	0.38	0.49	1.0000	1.0000	1.0000
	GRNN	0.95	2.84	4.16	0.9997	0.9973	0.9950
	ANFIS	0.23	0.66	3.66	1.0000	0.9998	0.9955
HAZ_{out}	SNN	1.14	2.10	2.23	0.9997	0.9993	0.9992
	5-hidden-layer DNN	0.25	0.35	0.38	1.0000	1.0000	1.0000
	GRNN	2.45	4.39	3.86	0.9984	0.9943	0.9951
	ANFIS	1.03	4.12	3.10	0.9992	0.9939	0.9966
Cp	SNN	1.83	2.39	0.89	0.9993	0.9989	0.9998
	5-hidden-layer DNN	0.23	0.34	0.23	1.0000	1.0000	1.0000
	GRNN	0.04	3.47	3.14	1.0000	0.9960	0.9979
	ANFIS	1.05	3.73	5.32	0.9993	0.9970	0.9942

4.6. Cut Quality Optimization Using Modified Equilibrium Optimizer (M-EO)

EO is a metaheuristic optimization technique inspired by the dynamic mass balance within a control volume [32]. The adjustment of particle concentration in EO primarily involves factors such as an equilibrium pool ($\vec{C}_{eq,pool}$), an exponential term (F), and a generation rate (G). A detailed explanation of the EO algorithm can be found in Reference [32]. In EO, implementing memory-saving techniques for particles aids in achieving an equilibrium state. This mechanism bears resemblance to PSO's P_{best} concept, where each particle's fitness value in the current iteration is evaluated against that of the previous iteration, and if it yields a better fit, it replaces the previous value. In this research, the memory-saving strategy was executed through the following procedure. Firstly, all particles of the previous iteration and the current iteration were combined. The combined particles were then sorted according to their fitness values. Next, the best particles were selected as the best-so-far ones. Furthermore, the top four of the best-so-far particles were then used as $\vec{C}_{eq(1)}$, $\vec{C}_{eq(2)}$, $\vec{C}_{eq(3)}$, and $\vec{C}_{eq(4)}$, respectively, in the updated equilibrium pool $\vec{C}_{eq,pool} = \left\{\vec{C}_{eq(1)}, \vec{C}_{eq(2)}, \vec{C}_{eq(3)}, \vec{C}_{eq(4)}, \vec{C}_{eq(ave)}\right\}$, where $\vec{C}_{eq(ave)} = \left(\vec{C}_{eq(1)} + \vec{C}_{eq(2)} + \vec{C}_{eq(3)} + \vec{C}_{eq(4)}\right)/4$.

In the optimization process for enhancing cut quality, the population comprised 200 particles, with a maximum number of iterations of 500. The variables including R, P, f, and v were confined within specific ranges: 0.5–6 mm, 11–18.6 W, 20–40 kHz, and 0.05–0.3 mm/s, respectively. Each particle's fitness was determined using the NCQ formula (Equation (1)). Subsequently, the 5-hidden-layer DNN was integrated with the M-EO to identify the optimal process parameters. Figure 10 illustrates the optimal and average fitness levels of all particles throughout each iteration. The evolution of fitness depicted in Figure 10 indicates that M-EO outperforms EO in attaining the equilibrium state, and the solutions obtained through M-EO are superior to those of EO. These outcomes underscore the enhancements achieved by the developed M-EO.

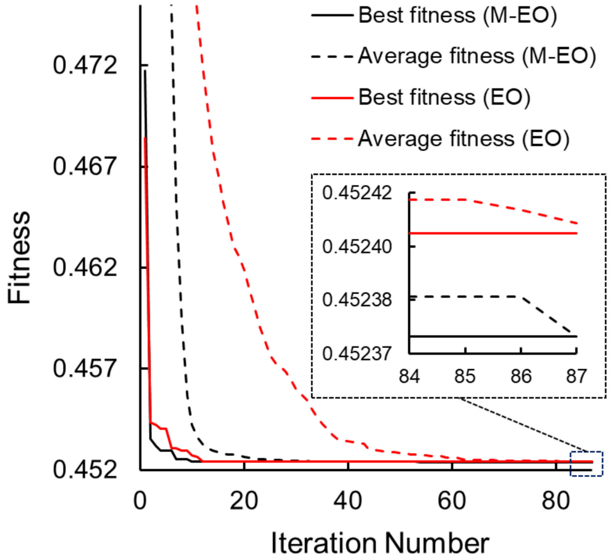

Figure 10. The best fitness and average fitness obtained by M-EO and EO.

The resulting optimal values for curvature radius, laser power, pulse frequency, and cutting speed were determined as 2.9 mm, 11.29 W, 26.04 kHz, and 0.27 mm/s, respectively. It is noteworthy that the optimal laser power (11.29 W) was lower than the lowest laser power used in the initial experiment (12 W), while the optimal cutting speed (0.27 mm/s) exceeded the highest cutting speed employed in the initial experiment (0.20 mm/s). This indicates that the optimal combination of laser process parameters fell outside the range explored in the initial laser cutting trials. The predicted optimal cut qualities corresponding to these parameters were 46.60 µm, 62.58 µm, 55.85 µm, and 0.021 for Kw, HAZ_{in}, HAZ_{out}, and Rp, respectively.

The predicted HAZ_{out} of 55.85 µm for the optimal cut quality slightly exceeded that of the most favorable cut quality sample (Experiment No. 34) from the initial trials, which measured 55.80 µm. Nevertheless, when the laser process parameters from Experiment No. 34 were applied, the predicted HAZ_{out} calculated by the 5-hidden-layer DNN model was 55.87 µm, suggesting that the predicted HAZ_{out} for Experiment No. 34 was less desirable compared to the optimal outcome. Conversely, while the optimal HAZ_{in} value (62.58 µm) surpassed that of Experiment No. 34 (62.12 µm) and the prediction for Experiment No. 34 (62.26 µm), the overall fitness of the optimal cut quality (0.4524) was lower than that of the specified Experiment No. 34 (0.4552). Therefore, the developed M-EO algorithm effectively identifies the optimal laser process parameters necessary to achieve the best cut quality.

4.7. Experimental Validation

Five validation experiments were repeatedly conducted for the optimal process parameters. The experimental validation results and comparisons with those in the initial Experiment No. 34 are summarized in Table 3. The comparisons show that an average improvement of 8.89%, 2.14%, 9.49%, and 83.08% was observed for Kw, HAZ_{in}, HAZ_{out}, and Rp, respectively, using the proposed optimization method. The average improvement for the jth quality index, as depicted in Table 3, is determined using the following formula:

$$\text{Average Improvement}_j = \frac{IE_j\text{-}AVE_j}{IE_j} \cdot 100\% \tag{6}$$

where IE_j represents the value of Initial Experiment No. 34 for the jth quality index, and AVE_j denotes the average value derived from five experimental validations for the same quality index.

Table 3. Experimental validation test results.

Quality Index	Validation Experiment No.					Prediction of Optimal Value	Initial Experiment No. 34	Average Improvement (%)
	1	2	3	4	5			
Kw (µm)	42.21	42.42	45.01	41.56	41.77	46.60	46.75	8.89
HAZ_{in} (µm)	60.91	60.92	60.51	61.08	60.52	62.58	62.12	2.14
HAZ_{out} (µm)	47.49	49.58	55.09	52.85	47.51	55.85	55.80	9.49
Rp	0.007	0.006	0	0	0.009	0.021	0.026	83.08

The proposed optimization method led to consistent improvements in Kw, HAZ_{in}, HAZ_{out}, and Rp, which were observed during validation experiments conducted with optimal laser process parameters. Specifically, for Kw, the validation experiments resulted in an average of 42.59 µm, representing an average improvement of 8.89% compared to initial experiment No. 34. Regarding HAZ_{in}, the validation experiments showed an average of 60.79 µm, reflecting an average improvement of 2.14% compared to the initial experiment. Similarly, for HAZ_{out}, the validation experiments yielded an average value of 50.50 µm, indicating an average improvement of 9.49% compared to the initial experiments. Lastly, for Rp, the validation experiments produced an average value of 0.004, indicating an average improvement of 83.08% compared to the initial experiment.

Furthermore, the straight cut was performed using the ideal laser power, pulse frequency, and cutting speed, which were identical to those used for the curved cut with a curvature radius of 2.9 mm. Both cuts had a length of 4.55 mm. The straight cut was made five times in a series of studies. Table 4 displays the measurements for kerf width (Kw), left side heat-affected zone (HAZ_{left}), right side heat-affected zone (HAZ_{right}), and re-welded portion (Rp). Table 4 demonstrates that the majority of experimental outcomes for straight cuts do not involve any re-welded portion, and these outcomes are comparable to those seen for curved cuts (Table 3).

Table 4. Results of straight cut using the optimal laser power, pulse frequency, and cutting speed.

Quality Index	Straight-Cut Experiment No.				
	1	2	3	4	5
Kw (µm)	41.77	40.44	40.55	41.74	41.39
HAZ_{left} (µm)	60.74	58.38	57.85	58.96	61.19
HAZ_{right} (µm)	58.26	57.51	56.20	59.75	56.86
Rp	0	0.013	0	0	0

Figure 11 illustrates the comparisons of kerf width (Kw) and HAZ between curved cuts and straight cuts, utilizing the optimal process settings. Figure 11a demonstrates that the average Kw of the straight cut was somewhat less compared to the curved cut. The interval plots of the curved cut in Figure 11b clearly demonstrate that HAZ_{in} is considerably greater than HAZ_{out}. This aligns with the information presented in Figure 4. However, the interval plots in Figure 11b indicate that there are no notable distinctions between HAZ_{left} and HAZ_{right}. The difference in HAZ between straight and curved cuts can be attributed to specific effects of beam trajectory in curved laser cutting. These effects include uneven distribution of beam energy, concentrated bulk heating of the material, as well as heat conduction converging near the center of rotation and diverging away from it [39].

The outcomes from the validation experiments for both the curved and straight cuts demonstrated the effectiveness and reliability of the combined 5-hidden-layer DNN and M-EO models. These models successfully identified an optimal set of laser process parameters, even beyond the specified process window from the initial experiments, resulting in significant enhancements. Notably, while the models were initially developed based on the results from curved cuts, they proved adaptable and capable of yielding comparable outcomes for straight cuts as well. Consequently, the methodologies introduced in this study offer a reliable approach for predicting the optimal laser process parameters and subsequently achieving the optimal cut quality in the laser cutting of thin non-oriented electrical steel sheets.

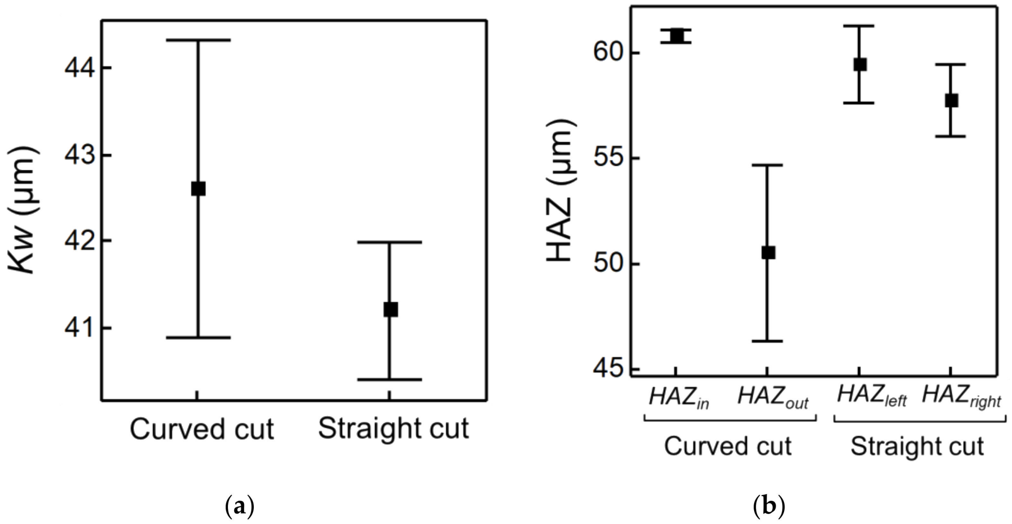

Figure 11. Interval plots illustrating (**a**) *Kw* and (**b**) HAZ for curved and straight cuts in laser cutting employing the optimal process parameters.

For comparison, the MAPE of prediction in various studies of laser cutting and machining is presented in Table 5. In addition, the process optimization method and the optimization constraints are also presented in Table 5 for some studies. The MAPE results in this study, compared to those obtained in other research and presented in Table 5, suggest the effectiveness of the proposed DNN-EO model in predicting cutting quality and optimizing the process. In addition to the DNN-EO model's capability to achieve superior prediction accuracy compared to other models, as evidenced in Table 5, a primary advantage of the models created in this study is their capacity to extend towards identifying optimal parameters beyond the initial experimental phase. These represent key advantages of the developed models.

Table 5. Comparison of MAPE of prediction and search space for optimization in various studies of laser cutting and machining.

References	Model	MAPE (%)	Optimization Method	Optimization Constraints
Rajamani et al. [14]	ANFIS-GA	1.01	WOA	Within the process window given in the initial experiments
Ding et al. [13]	GRNN	2.34	NSGA II	
Chaki et al. [40]	ANN	1.06	PSO	
Vagheesan et al. [41]	ANN	0.60	GA	
Yang et al. [42]	ANN	<7.00	GA	
Kechagias et al. [12]	ANN	9.83	-	-
Alajmi and Almeshal [43]	ANFIS-QPSO	4.95	-	-
This study	DNN-EO	0.38	M-EO	Beyond the process window given in the initial experiments

The MAPE of this study shown in Table 5 is the average of training, validation, and testing. Rajamani et al. [14] employed a hybrid ANFIS-GA approach to forecasting three quality metrics during the laser cutting of Hastelloy C276 sheets. Additionally, in their study, Rajamani et al. [14] employed a whale optimization algorithm (WOA) to determine the optimal laser process parameters. In another investigation, a GRNN was employed in conjunction with a non-dominated sorting GA (NSGA) II algorithm to both predict and optimize kerf width and surface roughness in the laser machining of 304L stainless steel plates [13]. Other studies have utilized various optimization techniques such as PSO and ANN [40] as well as GA and ANN [41] to enhance cut quality in the laser cutting of aluminum alloy sheets.

Yang et al. [42] utilized ANN and GA to forecast and optimize surface roughness during the machining of graphite/polymer composite. In a separate study, Kechagias et al. [12] employed an ANN to predict four quality metrics in the laser-cutting process of PMMA sheets. Alajmi and Almeshal [43] employed a quantum PSO (QPSO) algorithm to identify the optimal ANFIS parameters for predicting surface roughness in the machining of AISI 304. The performance of the DNN-EO model developed in this study surpasses that of other comparative AI-based models in various studies, as indicated by the MAPE values in Table 5. Furthermore, the focus of prior studies [12–14,40–43] was solely on identifying the optimal laser process parameters within the provided experimental conditions. In contrast, the models developed in this study can extend to identifying the optimal parameters beyond the initial experimental window. The comprehensive comparison demonstrates the superiority of the models developed in this study over those in previous research [12–14,40–43], highlighted by the smaller MAPE value and their capability to identify optimal process parameters beyond the initially provided experimental range.

5. Conclusions

The curved laser cutting of thin non-oriented electrical steel sheets in an oil environment was investigated utilizing a pulsed fiber laser system. To predict and optimize various aspects of cut quality, an efficient 5-hidden-layer DNN model and a modified EO algorithm were created. The cut quality was characterized by four key indices: kerf width, inner HAZ, outer HAZ, and re-welded portion. Insights drawn from the outcomes are summarized as follows.

1. The significant effect of each controlled laser process parameter on cut quality was validated using RFM and RSM. Thus, they were suitably used as inputs for the AI-based models. The RFM results showed that laser pulse frequency was the most important variable affecting cut quality, followed by laser power, curvature radius, and cutting speed.
2. The 5-hidden-layer DNN emerged as the most accurate among the developed DNNs, showcasing superior performance compared to the SNN, GRNN, and ANFIS models. It demonstrated exceptional effectiveness with remarkably low MAPE values and exceptionally high R^2 values across the training, validation, and testing datasets.
3. The M-EO, in conjunction with the 5-hidden-layer DNN, was employed to determine the most favorable laser process parameters for achieving the highest quality cut. The advanced M-EO has the capability to identify the most effective laser process settings in order to get a superior cut quality compared to the results obtained in the initial experiments. Based on the fitness evolution, M-EO achieved equilibrium before EO, and the solution obtained using M-EO was superior to that obtained using EO, demonstrating the superiority of M-EO over EO.
4. The validation experiments for both curved and straight cuts confirmed the reliability and robustness of the models created in this study. These models effectively produced the best cut quality and demonstrated significant enhancements across all quality indices. Thus, the methods proposed herein offer a reliable means of predicting the optimal laser process parameters and achieving the resulting optimal cut quality for the laser cutting of thin non-oriented electrical steel sheets.
5. The DNN and M-EO models developed in this study exhibit superior performance compared to those in previous research, particularly in terms of MAPE value. The proposed DNN model achieved a lower MAPE value, indicating its higher accuracy in predicting cut quality. Additionally, the M-EO model demonstrated the capability to identify optimal process parameters that extend beyond the predefined window of initial experiments, resulting in the attainment of optimal cut quality.

Supplementary Materials: The following supporting information can be downloaded at https://doi.org/10.5281/zenodo.10843642, Table S1: Full factorial combination of laser process parameters and experimental results.

Author Contributions: Conceptualization, M.N.R. and C.-K.L.; methodology, C.-K.L., C.-T.L., J.-R.H. and P.-C.T.; investigation, M.N.R.; resources, C.-K.L., C.-T.L., J.-R.H. and P.-C.T.; data curation, M.N.R. and C.-K.L.; writing—original draft preparation, M.N.R.; writing—review and editing, C.-K.L.; project administration, C.-K.L.; funding acquisition, C.-K.L. All authors have read and agreed to the published version of the manuscript.

Funding: This research was funded by the Ministry of Science and Technology (Taiwan) under Contract Nos. MOST 110-2221-E-008-089 and 111-2221-E-008-001.

Institutional Review Board Statement: Not applicable.

Informed Consent Statement: Not applicable.

Data Availability Statement: The data presented in this study are included in the Supplementary Materials.

Conflicts of Interest: The authors declare no conflicts of interest. The funder had no role in the design of the study; in the collection, analyses, or interpretation of data; in the writing of the manuscript or in the decision to publish the results.

References

1. Zhang, Y.X.; Lan, M.F.; Wang, Y.; Fang, F.; Lu, X.; Yuan, G.; Misra, R.D.K.; Wang, G.D. Microstructure and texture evolution of thin-gauge non-oriented silicon steel with high permeability produced by twin-roll strip casting. *Mater. Charact.* **2019**, *150*, 118–127. [CrossRef]
2. Siebert, R.; Schneider, J.; Beyer, E. Laser cutting and mechanical cutting of electrical steels and its effect on the magnetic properties. *IEEE Trans. Magn.* **2014**, *50*, 2001904. [CrossRef]
3. Saleem, A.; Alatawneh, N.; Rahman, T.; Lowther, D.A.; Chromik, R.R. Effects of laser cutting on microstructure and magnetic properties of non-orientation electrical steel laminations. *IEEE Trans. Magn.* **2020**, *56*, 6100619. [CrossRef]
4. Nguyen, T.-H.; Lin, C.-K.; Tung, P.-C.; Nguyen-Van, C.; Ho, J.-R. Artificial intelligence-based modeling and optimization of heat-affected zone and magnetic property in pulsed laser cutting of thin nonoriented silicon steel. *Int. J. Adv. Manuf. Technol.* **2021**, *113*, 3225–3240. [CrossRef]
5. Schleier, M.; Adelmann, B.; Esen, C.; Hellmann, R. Image processing algorithm for in situ monitoring fiber laser remote cutting by a high-speed camera. *Sensors* **2022**, *22*, 2856. [CrossRef] [PubMed]
6. Sharma, A.; Yadava, V. Experimental analysis of Nd-YAG laser cutting of sheet materials—A review. *Opt. Laser Technol.* **2018**, *98*, 264–280. [CrossRef]
7. Rohman, M.N.; Ho, J.-R.; Tung, P.-C.; Tsui, H.-P.; Lin, C.-K. Prediction and optimization of geometrical quality for pulsed laser cutting of non-oriented electrical steel sheet. *Opt. Laser Technol.* **2022**, *149*, 107847. [CrossRef]
8. Nguyen, D.-T.; Ho, J.-R.; Tung, P.-C.; Lin, C.-K. An improved real-time temperature control for pulsed laser cutting of non-oriented electrical steel. *Opt. Laser Technol.* **2021**, *136*, 106783. [CrossRef]
9. Nguyen, D.-T.; Ho, J.-R.; Tung, P.-C.; Lin, C.-K. Prediction of Kerf width in laser cutting of thin non-oriented electrical steel sheets using convolutional neural network. *Mathematics* **2021**, *9*, 2261. [CrossRef]
10. Madić, M.; Mladenović, S.; Gostimirović, M.; Radovanović, M.; Janković, P. Laser cutting optimization model with constraints: Maximization of material removal rate in CO_2 laser cutting of mild steel. *Proc. Inst. Mech. Eng. Part B J. Eng. Manuf.* **2020**, *234*, 1323–1332. [CrossRef]
11. Rohman, M.N.; Ho, J.-R.; Tung, P.-C.; Lin, C.-T.; Lin, C.-K. Prediction and optimization of dross formation in laser cutting of electrical steel sheet in different environments. *J. Mater. Res. Technol.* **2022**, *18*, 1977–1990. [CrossRef]
12. Kechagias, J.D.; Tsiolikas, A.; Petousis, M.; Ninikas, K.; Vidakis, N.; Tzounis, L. A robust methodology for optimizing the topology and the learning parameters of an ANN for accurate predictions of laser-cut edges surface roughness. *Simul. Model. Pract. Theory* **2022**, *114*, 102414. [CrossRef]
13. Ding, H.; Wang, Z.; Guo, Y. Multi-objective optimization of fiber laser cutting based on generalized regression neural network and non-dominated sorting genetic algorithm. *Infrared Phys. Technol.* **2020**, *108*, 103337. [CrossRef]
14. Rajamani, D.; Siva Kumar, M.; Balasubramanian, E.; Tamilarasan, A. Nd: YAG laser cutting of Hastelloy C276: ANFIS modeling and optimization through WOA. *Mater. Manuf. Process.* **2021**, *36*, 1746–1760. [CrossRef]
15. Sibalija, T.; Petronic, S.; Milovanovic, D. Experimental optimization of Nimonic 263 laser cutting using a particle swarm approach. *Metals* **2019**, *9*, 1147. [CrossRef]
16. Guo, J.; Wang, B.; He, Z.X.; Pan, B.; Du, D.X.; Huang, W.; Kang, R.K. A novel method for workpiece deformation prediction by amending initial residual stress based on SVR-GA. *Adv. Manuf.* **2021**, *9*, 483–495. [CrossRef]

17. Elsheikh, A.H.; Shehabeldeen, T.A.; Zhou, J.; Showaib, E.; Abd Elaziz, M. Prediction of laser cutting parameters for polymethylmethacrylate sheets using random vector functional link network integrated with equilibrium optimizer. *J. Intell. Manuf.* **2021**, *32*, 1377–1388. [CrossRef]
18. Yilbas, B.S.; Arif, A.F.M.; Abdul Aleem, B.J. Laser cutting of sharp edge: Thermal stress analysis. *Opt. Lasers Eng.* **2010**, *48*, 10–19. [CrossRef]
19. Pandey, A.K.; Gautam, G.D. Grey relational analysis-based genetic algorithm optimization of electrical discharge drilling of Nimonic-90 superalloy. *J. Braz. Soc. Mech. Sci. Eng.* **2018**, *40*, 117. [CrossRef]
20. Hamad, A.H. Effects of different laser pulse regimes (nanosecond, picosecond and femtosecond) on the ablation of materials for production of nanoparticles in liquid solution. In *High Energy Short Pulse Lasers*; Viscup, R., Ed.; IntechOpen: London, UK, 2016; pp. 305–325. [CrossRef]
21. Chelgani, S.C.; Matin, S.S.; Hower, J.C. Explaining relationships between coke quality index and coal properties by random forest method. *Fuel* **2016**, *182*, 754–760. [CrossRef]
22. Saffaran, A.; Moghaddam, M.A.; Kolahan, F. Optimization of backpropagation neural network-based models in EDM process using particle swarm optimization and simulated annealing algorithms. *J. Braz. Soc. Mech. Sci. Eng.* **2020**, *42*, 73. [CrossRef]
23. Kumar, R.; Bilga, P.S.; Singh, S. Multi objective optimization using different methods of assigning weights to energy consumption responses, surface roughness and material removal rate during rough turning operation. *J. Clean. Prod.* **2017**, *164*, 45–57. [CrossRef]
24. Rodnight, R. Manometric determination of the solubility of oxygen in liquid paraffin, olive oil and silicone fluids. *Biochem. J.* **1954**, *57*, 661–663. [CrossRef] [PubMed]
25. Riveiro, A.; Quintero, F.; Lusquiños, F.; Comesaña, R.; Del Val, J.; Pou, J. The role of the assist gas nature in laser cutting of aluminum alloys. *Phys. Procedia* **2011**, *12*, 548–554. [CrossRef]
26. Yilbas, B.S.; Abdul Aleem, B.J. Dross formation during laser cutting process. *J. Phys. D Appl. Phys.* **2006**, *39*, 1451–1461. [CrossRef]
27. Muhammad, N.; Whitehead, D.; Boor, A.; Li, L. Comparison of dry and wet fibre laser profile cutting of thin 316L stainless steel tubes for medical device applications. *J. Mater. Process. Technol.* **2010**, *210*, 2261–2267. [CrossRef]
28. Feng, S.; Zhou, H.; Dong, H. Using deep neural network with small dataset to predict material defects. *Mater. Des.* **2019**, *162*, 300–310. [CrossRef]
29. Prakash, J.; Kankar, P.K. Health prediction of hydraulic cooling circuit using deep neural network with ensemble feature ranking technique. *Measurement* **2020**, *151*, 107225. [CrossRef]
30. Agarap, A.B. Deep learning using rectified linear units (ReLU). *arXiv* **2019**, arXiv:1803.08375. [CrossRef]
31. Pennington, J.; Schoenholz, S.S.; Ganguli, S. Resurrecting the sigmoid in deep learning through dynamical isometry: Theory and practice. *arXiv* **2017**, arXiv:1711.04735. [CrossRef]
32. Faramarzi, A.; Heidarinejad, M.; Stephens, B.; Mirjalili, S. Equilibrium optimizer: A novel optimization algorithm. *Knowl. Based Syst.* **2020**, *191*, 105190. [CrossRef]
33. Liu, G.; Bao, H.; Han, B. A stacked autoencoder-based deep neural network for achieving gearbox fault diagnosis. *Math. Probl. Eng.* **2018**, *2018*, 5105709. [CrossRef]
34. Kang, S.-J.; Fan, J.-H.; Mao, W.; Wu, Q.; Feng, J.; Yin, Y. Evaluating the optical classification of *fermi* BCUs using machine learning. *Astrophys. J.* **2019**, *872*, 189. [CrossRef]
35. Picard, R.R.; Cook, R.D. Cross-validation of regression models. *J. Am. Stat. Assoc.* **1984**, *79*, 575–583. [CrossRef]
36. Jafarian, F.; Amirabadi, H.; Sadri, J. Integration of finite element simulation and intelligent methods for evaluation of thermo-mechanical loads during hard turning process. *Proc. Inst. Mech. Eng. Part B J. Eng. Manuf.* **2013**, *227*, 235–248. [CrossRef]
37. Shivakoti, I.; Kibria, G.; Pradhan, P.M.; Pradhan, B.B.; Sharma, A. ANFIS based prediction and parametric analysis during turning operation of stainless steel 202. *Mater. Manuf. Process.* **2019**, *34*, 112–121. [CrossRef]
38. Mathew, J.; Griffin, J.; Alamaniotis, M.; Kanarachos, S.; Fitzpatrick, M.E. Prediction of welding residual stresses using machine learning: Comparison between neural networks and neuro-fuzzy systems. *Appl. Soft Comput. J.* **2018**, *70*, 131–146. [CrossRef]
39. Sheng, P.; Cai, L.H. Predictive process planning for laser cutting. *J. Manuf. Syst.* **1998**, *17*, 144–158. [CrossRef]
40. Chaki, S.; Bose, D.; Bathe, R.N. Multi-objective optimization of pulsed Nd: YAG laser cutting process using entropy-based ANN-PSO model. *Lasers Manuf. Mater. Process.* **2020**, *7*, 88–110. [CrossRef]
41. Vagheesan, S.; Govindarajalu, J. Hybrid neural network–particle swarm optimization algorithm and neural network–genetic algorithm for the optimization of quality characteristics during CO_2 laser cutting of aluminum alloy. *J. Braz. Soc. Mech. Sci. Eng.* **2019**, *41*, 328. [CrossRef]
42. Yang, D.; Guo, Q.; Wan, Z.; Zhang, Z.; Huang, X. Surface roughness prediction and optimization in the orthogonal cutting of graphite/polymer composites based on artificial neural network. *Processes* **2021**, *9*, 1858. [CrossRef]
43. Alajmi, M.S.; Almeshal, A.M. Prediction and optimization of surface roughness in a turning process using the ANFIS-QPSO method. *Materials* **2020**, *13*, 2986. [CrossRef] [PubMed]